

Article

CoFe₂O₄/MoS₂@Au: Multifunction Z-Scheme Heterojunction for SERS Monitoring and Photocatalytic Degradation of Fungicides

Qirong Dong^{1,2,3} , Qingyi Wei^{1,2,3,*} and Hongbin Pu^{1,2,3,*} ¹ School of Food Science and Engineering, South China University of Technology, Guangzhou 510641, China² Academy of Contemporary Food Engineering, South China University of Technology, Guangzhou Higher Education Mega Centre, Guangzhou 510006, China³ Engineering and Technological Research Centre of Guangdong Province on Intelligent Sensing and Process Control of Cold Chain Foods, & Guangdong Province Engineering Laboratory for Intelligent Cold Chain Logistics Equipment for Agricultural Products, Guangzhou Higher Education Mega Centre, Guangzhou 510006, China

* Correspondence: feweiqingyi@scut.edu.cn (Q.W.); fehbpu@scut.edu.cn (H.P.)

Abstract: Efficient detection and degradation of fungicides are greatly concerned with aquatic food safety. Herein, a multifunction CoFe₂O₄/MoS₂@Au (ACMS) composite was synthesized for crystal violet (CV) and malachite green (MG) photocatalytic degradation and SERS determination. As the construction of the Z-scheme heterostructure of ACMS, which enhanced the light absorption capability and the separation efficiency of photoexcited carrier significantly, ACMS possessed an excellent photocatalytic performance with a degradation rate of 94.76% for CV under simulated solar light irradiation. Furthermore, the multifunction ACMS exhibited superior SERS capability with a detection limit (LOD) of $4.309 \times 10^{-2} \mu\text{g L}^{-1}$ for MG residues in water. And the ACMS substrates could be utilized to determine the MG residues in crucian carp extract, resulting in a recovery rate of 96.00~116.00%. In addition, such multifunction heterojunctions were performed for in situ monitoring of the photodegradation process. This research opened up a novel perspective on the applications of heterojunction-based multifunction materials for food safety control.

Keywords: aquatic food safety; SERS; photocatalytic; Z-scheme heterojunction; fungicides



Citation: Dong, Q.; Wei, Q.; Pu, H. CoFe₂O₄/MoS₂@Au: Multifunction Z-Scheme Heterojunction for SERS Monitoring and Photocatalytic Degradation of Fungicides. *Separations* **2023**, *10*, 526. <https://doi.org/10.3390/separations10100526>

Academic Editor: Dimosthenis Giokas

Received: 25 August 2023

Revised: 18 September 2023

Accepted: 20 September 2023

Published: 28 September 2023



Copyright: © 2023 by the authors. Licensee MDPI, Basel, Switzerland. This article is an open access article distributed under the terms and conditions of the Creative Commons Attribution (CC BY) license (<https://creativecommons.org/licenses/by/4.0/>).

1. Introduction

Aquatic food security is one of most the tremendous issues faced worldwide. The increasing challenges in aquatic food security due to the abuse of fungicides including malachite green (MG) and crystal violet (CV) have attracted growing attention [1]. This is concerning, as even tiny amounts of fungicides can be enriched efficiently through the food chain and significantly threaten human health [2]. Facing this urgent problem, it is essential to find a novel way to construct effective fungicide detection and degradation strategies for food safety.

Determination of fungicide residues in aquaculture is a significant part of the food safety protection system [3]. Surface-enhanced Raman scattering (SERS) has been widely utilized for food contaminants determination owing to its merits including simple pretreatment, cost-effectiveness and less time consumption [4]. In addition, the decomposition of fungicides is also essential in the face of the diversification food contaminants problem. Hitherto, various technologies involving adsorption, ion exchange, microbiological decomposition and photocatalysis have been employed to resolve the food contamination problem [5]. Among them, photocatalysis, as a modern green and energy-saving technique, has dramatically advanced the revolution of food contaminants treatment methods for its high degradation rate and mineralization efficiency [6]. However, using SERS and photocatalytic techniques, it is still difficult to realize the diversified needs of practical

applications due to their intrinsic defects such as instability, poor sensitivity and limited catalytic efficiency. By virtue of photocatalytic performance and SERS activity, multifunction materials have been designed for determining and degrading contaminants, which exhibits great prospects for comprehensive aquatic food safety control [7].

Molybdenum disulfide (MoS_2), with the advantages of non-toxicity, high stability, fascinating light-responded bandgaps, superior electron conductivity, unique layered structures, etc., has drawn global attention to its application in detection and catalysis fields [8]. A case in point, Govarthan and co-workers proposed MoS_2 @MIL-88(Fe) composites for photodegradation of methylene blue (MB) [9]. The as-prepared MoS_2 -based materials possessed a degradation efficiency of 98.5%. In addition, by virtue of MoS_2 nanomaterials, a series of SERS substrates constructed with other semiconductors or metals have been designed for the enhancement of SERS performance. For instance, Quan, et al. [10] proposed a $\text{MoS}_2/\text{TiO}_2$ substrate for MG determination. As a result, such MoS_2 -based substrates could realize the analysis of MG in water with a detection limit of 10^{-10} M. In this regard, MoS_2 exhibits intriguing prospects in the fabrication of multifunctional materials for food contaminants monitoring and degradation.

On the other hand, the fast recombination of photogenerated carriers and limited SERS activity still inhibit the practical applications of MoS_2 in food contaminants control. Heterojunction construction is considered a potential method to solve the aforementioned problem. Specifically, the heterojunctions can enhance solar light absorption and decrease the recombination of photoexcited electron-hole pairs. The Z-scheme heterojunction, in particular, has received extensive attention in recent years as a result of its redox potential. Meanwhile, the recombination of photogenerated carriers can be further restrained owing to its unique heterostructure [11]. For instance, Liu, et al. [12] prepared a Ag/AgVO₃/carbon-rich g-C₃N₄ heterojunction, which effectively enhanced the photodegradation capability of sulfamethiadiazole ($k = 0.1504 \text{ min}^{-1}$), illustrating the superiority of the Z-scheme heterostructure. Whereas, there is scarce research focused on the use of Z-scheme heterostructure-based multifunction materials for fungicide control.

As a novel bimetallic oxide, CoFe_2O_4 has been explored and applied to fabricate heterojunctions due to its fascinating redox, photocatalytic, and magnetic capabilities. However, the magnetic performance makes it easier to self-aggregate, which significantly decreases its catalytic property [13]. The utilization of CoFe_2O_4 and MoS_2 to prepare heterojunction can effectively impair its self-aggregation, and improve the transfer of photocatalytic carriers [14]. Thus, CoFe_2O_4 combined with MoS_2 for the construction of Z-scheme heterojunction is an attractive issue in multifunction materials developing roads. Additionally, the virtues of noble metal nanoparticles involving surface plasmon resonance (SPR) effect and localized surface plasmon resonance (LSPR) property have inspired the researchers to construct ternary Z-scheme heterojunctions, which can further enhance the SERS effect and solar light absorption capability [15].

Herein, gold nanoparticles (AuNPs) were carried out as an electron mediator to couple CoFe_2O_4 and MoS_2 to fabricate a $\text{CoFe}_2\text{O}_4/\text{MoS}_2$ @Au (ACMS) Z-scheme heterojunction. The synthesized multifunction composites exhibited excellent SERS sensitivity and allowed to determine MG with a detection limit of $4.309 \times 10^{-2} \mu\text{g mL}^{-1}$. And such heterojunction could be performed to detect fungicides in fish extract. Additionally, the light absorption and photogenerated carriers' migration capability of ACMS composites is enhanced significantly due to the fabrication of a Z-scheme heterostructure, which could be employed to degrade 94.76% of CV within 90 min under simulated light irradiation. Furthermore, the ACMS heterojunction was utilized for real-time monitoring of the photodegradation process. Attributed to the detection and degradation capabilities, the synthesized ACMS may blaze a new trail for food safety comprehensive control.

2. Experimental

2.1. Reagents and Materials

Isopropyl alcohol (IPA), iron (III) chloride ($\text{FeCl}_3 \cdot 6\text{H}_2\text{O}$), cobalt (II) chloride ($\text{CoCl}_2 \cdot 6\text{H}_2\text{O}$), thiourea ($\text{CH}_4\text{N}_2\text{S}$), sodium acetate (CH_3COONa), ethylene glycol (EG) (CH_2OH)₂, polyethylene glycol-8000 (PEG-8000), p-benzoquinone (p-BQ), and hexaammonium molybdate ($(\text{NH}_4)_6\text{Mo}_7\text{O}_{27}$) were bought from Macklin Biochemical Technology Co., Ltd. (Shanghai, China). Chloroauric acid trihydrate ($\text{HAuCl}_4 \cdot 3\text{H}_2\text{O}$), ethylenediaminetetraacetic acid disodium salt (EDTA-2Na), sodium acetate (CH_3COONa), crystal violet, malachite green, and trisodium citrate dihydrate ($\text{Na}_3\text{Cit} \cdot 3\text{H}_2\text{O}$) were purchased from Sigma-Aldrich Co., Ltd. (Shanghai, China).

2.2. Instruments

The morphology, surface functional groups and crystal phase of as-synthesized materials were characterized by scanning electron microscopy (SEM) (Merlin, Carl Zeiss NTS GmbH, Oberkochen, Germany), high-resolution transmission electron microscope (HRTEM) (JEM-2100F Plus, JEOL Ltd., Tokyo, Japan), Fourier transform infrared spectra (FT-IR) (FT9700, Thermo-Nicolet Co., Waltham, MA, USA), and X-ray diffraction (XRD) (Empyrean, PANalytical B.V., Almelo, The Netherlands), respectively.

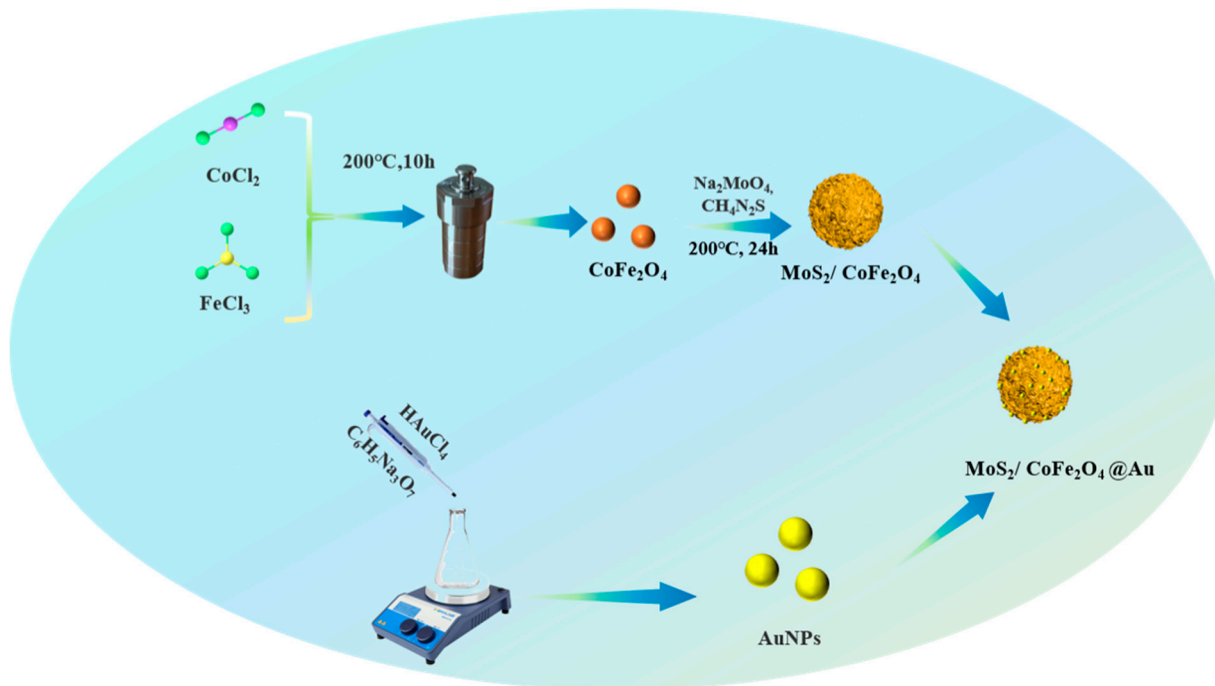
The UV-vis spectra and photoluminescence (PL) spectra were acquired by the UV-vis spectrophotometer (UV-1800, Shimadzu Co., Kyoto, Japan) and fluorescence spectrophotometer (RF-6000, Shimadzu Co., Kyoto, Japan), respectively. The SERS detection was performed with a laser confocal microscope Raman system (LabRAM HR, Horiba France SAS, Villeneuve d'Ascq, France) equipped with visible light (633 nm). The Zeta potential of as-prepared samples was investigated by particle and molecular size analyzer (Zetasizer Nano ZS, Malvern Instruments Ltd., Melvin, UK). The X-ray photoelectron spectroscopy (XPS, Axis Ultra DLD, Kratos Analytical Ltd., Manchester, UK) was carried out to research the chemical composition of materials. The electrochemical impedance spectra (EIS) were detected via an electro-chemical workstation (CHI660E, CH Instruments Co., Shanghai, China). A 500 W Xenon lamp (CEL-S500-T5, China Education Au-light Co., Beijing, China) was utilized as the source of simulated solar light (light source diameter: 50 mm, 100 mW cm^{-2}). The transient photocurrents were analyzed by an electrochemical workstation equipped with a 300 W Xe lamp (PLS-SXE300D, Beijing Perfect Light Technology Co., Ltd., Beijing, China).

2.3. Synthesis of $\text{CoFe}_2\text{O}_4/\text{MoS}_2@Au$

Preparation of CoFe_2O_4 [16]: 5 mmol of $\text{FeCl}_3 \cdot 6\text{H}_2\text{O}$ and 2.5 mmol of $\text{CoCl}_2 \cdot 6\text{H}_2\text{O}$ were dispersed in 40 mL ethylene glycol, and stirring with magnetic separator racks (C-MAG HS 7, IKA (Guangzhou, China) Instrument Equipment Co., Ltd., Guangzhou, China). Subsequently, 1.0 g PEG and 3.6 g CH_3COONa were gradually added to the previously prepared solution. The resulting solution was then transferred to Teflon-lined stainless steel autoclaves (YZ-100 mL, Shanghai Yanzheng Instrument Co., Ltd., Shanghai, China) and heated in a drying oven (DHG-9055, Shanghai Yiheng Scientific Instrument Co., Ltd., Shanghai, China) at 200°C for 10 h. The synthesized CoFe_2O_4 was subjected to centrifugation (10,000 rpm, 12 min) (JW-3024HR, Anhui Jiaven Equipment Industry Co., Ltd., Hefei, China) and washed alternately with ultrapure water and ethanol several times until the supernatant was colorless. The obtained materials were dried at 60°C overnight.

Fabrication of $\text{CoFe}_2\text{O}_4/\text{MoS}_2$ (CMS): $\text{CoFe}_2\text{O}_4/\text{MoS}_2$ was synthesized via the hydrothermal method as reported previously [17]. In detail, 0.420 g $(\text{NH}_4)_6\text{Mo}_7\text{O}_{24} \cdot 4\text{H}_2\text{O}$ and 0.912 g thiourea were dissolved in 60 mL ultrapure water and stirred for 20 min. Then, 0.1254 g CoFe_2O_4 was dispersed into the mixture and added to Teflon reactors (100 mL). After the reaction proceeded at 180°C for 10 h, black products were purified with ethanol and water thoroughly, and dried at 60°C , the as-prepared samples were noted as CMS.

Modification of AuNPs: At first, the AuNPs were fabricated via the previously reported method [18]. Next, the as-synthesized CMS composite was mixed with 5 mL AuNPs and treated with ultrasonic for 10–60 min. Finally, the as-prepared heterojunctions were centrifugated and dried, which were denoted as ACMS (Scheme 1).



Scheme 1. Schematic diagram of the synthesis procedure of ACMS.

2.4. Photocatalytic Degradation

The photodegradation efficiency of the as-prepared materials was estimated by analyzing the photocatalytic degradation of CV (37.5 mg L^{-1} , 40 mL and 20 mg photocatalysts) under simulated solar light irradiation [19]. Before the photocatalytic reaction, adsorption tests were mechanically stirred in the dark for half an hour to ensure adsorption equilibrium. The UV-vis spectrum was carried out to determine the absorption value of CV in the photodegradation process. And the absorption maximum of CV (590 nm) was performed to determine the concentration of CV. The degradation rate was evaluated according to the Equation (1):

$$\eta (\%) = (C_0 - C) / C_0 \times 100\% \tag{1}$$

Here, C_0 refers to the initial concentration of the CV solution, C represents the remaining CV concentration, and η stands for the photodegradation efficiency.

2.5. The Water Remediation Capability

Seed germination experiments were carried out to estimate the water remediation capability of ACMS heterojunction. Sixteen vigna radiata seeds were cultivated in each water sample including uncontaminated water, CV contaminated water (37.5 mg L^{-1}) and remediated water under room temperature, respectively. Then, the germination rate (SGR) and average root lengths (ARL) of seeds were determined after 7 days [20]. Furthermore, the seed germination indexes (SGI) were recorded by the following formula:

$$\text{SGI} = \frac{\text{SGR}_{cv} \% \times \text{ARL}_{cv}}{\text{SGR}_{dw} \% \times \text{ARL}_{dw}} \times 100\% \tag{2}$$

2.6. Evaluation of SERS Activity and Analysis Procedures for Fungicides

Crystal violet was chosen as the SERS label to justify the enhancement factor, sensitivity, and reproducibility of the ACMS multifunction composite. Firstly, 5 mg of ACMS heterojunction was dissolved in 2.4 mL water for the following determination. Then, 25 μ L CV was mixed with an equal amount of the ACMS solution. Next, a part of the mixture was sucked by a capillary and detected with Raman spectra. And the SERS detection of the MG residues was carried out under similar conditions.

2.7. In Situ Monitoring the Photodegradation Process

Firstly, 1 mL MG solution (final concentration: 0.1 mg/L) was utilized as the analytes and mixed with 1 mL ACMS heterojunction (5 mg/2.4 mL). For in situ monitoring of the photodegradation process, the above solution was irradiated with the Xe lamp (500 W), and recorded with Raman spectra each 10 min until no Raman peak could be observed.

2.8. Application to Actual Samples

For actual sample determination, the crucian carp were treated as previously reported [21]. Firstly, the crucian carp (2 ± 0.05 g) was washed with 0.5 mL hydroxylamine hydrochloride solution (9.5 g/L). Next, 1 g anhydrous magnesium sulfate and 10 mL acetonitrile were added into the crucian carp samples, keeping vortexed for 1 min. Then, 4 g neutral alumina was dispersed in solutions and vortexed for 2 min. The supernatant was centrifuged at 4000 rpm for 5 min, followed by drying in a water bath (50 °C) with nitrogen blow. The crucian carp samples were redispersed in acetonitrile solution (1 mL) and diluted with water (9.0 mL). Finally, the above-mentioned solution was mixed with MG and filtered through a 0.22 μ m hydrophobic polyvinylidene fluoride filter to collect the crucian carp extract. SERS intensities were determined as described previously.

2.9. Statistical Analysis

Tests were performed thrice and data were processed utilizing Origin 2020 software (OriginLab Co., Northampton, MA, USA). Raman spectrum analysis was conducted with LabSpec6 software (<https://www.horiba.com/int/scientific/products/detail/action/show/Product/labspec-6-spectroscopy-suite-software-1843/>) (accessed on 24 August 2023) (Horiba France SAS, Villeneuve d'Ascq, France).

3. Results and Discussion

3.1. Characterization of As-Prepared Samples

SEM and HRTEM characterizations were implemented to observe the morphology of CoFe_2O_4 , CMS and ACMS. As depicted in Figure 1A, the pure CoFe_2O_4 presented the aggregation statue due to the magnetic properties, and the spherical morphology of CoFe_2O_4 could be observed in the HRTEM figure (Figure 1E). In addition, the CMS materials exhibited a flower structure with a uniform size distribution of about 500 nm (Figure 1B), which was well in accordance with the corresponding HRTEM picture (Figure 1F). Furthermore, it could be found that the MoS_2 was covered with CoFe_2O_4 . As seen in Figure 1G, the hetero-interface boundary of CoFe_2O_4 and MoS_2 could be observed clearly and the 0.243 nm lattice fringe spacing represented the (220) plane of CoFe_2O_4 , while the interlayer spacing of 0.626 nm could be ascribed to the (002) planes for MoS_2 . As shown in Figure 1C,H, AuNPs could be modified outside of CMS with ultrasound-assisted deposition. The EDS mapping illustrated that the Fe, Co, Mo, S and Au elements were distributed uniformly (Figure 1D). The aforementioned results verified the construction of the ACMS heterojunction.

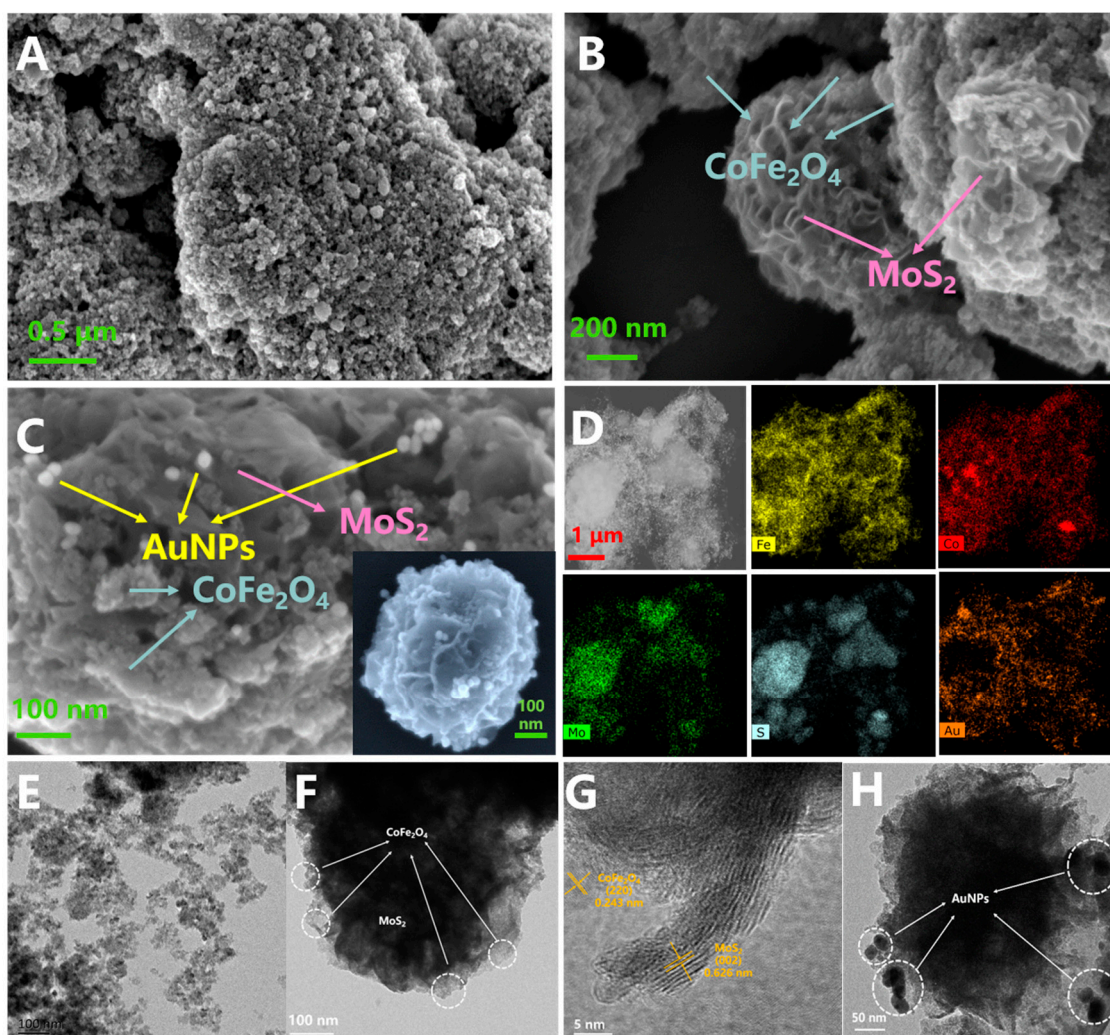


Figure 1. Characterization of the as-prepared samples. The SEM images of (A) CoFe_2O_4 , (B) CMS and (C) ACMS. (D) The elemental distribution maps of ACMS. The HRTEM images of (E) CoFe_2O_4 , (F,G) CMS and (H) ACMS.

As depicted in Figure 2A, the zeta potentials of CoFe_2O_4 , CMS and ACMS were 23.4, -17.2 and -21 mV, respectively. And the decrease in zeta potential further indicated the successful modification of AuNPs. Figure 2B exhibited the XRD diffraction patterns of as-prepared CoFe_2O_4 , CMS and ACMS photocatalysts. As for CoFe_2O_4 , four typical peaks located at 30.06 , 35.43 , 43.05 and 62.58° could be observed, which were ascribed to (220), (311), (400) and (440) planes, respectively. And MoS_2 showed excellent crystal structure with significant characteristic peaks at 31.2 and 57.18° , which could be attributed to its (100) and (110) planes, respectively. Meanwhile, the main characteristic peaks of 38.26 , 44.47 , 64.7 and 77.45° in the ACMS curve were ascribed to the (111), (200), (220) and (311) planes of AuNPs, respectively. And the intensity of each diffraction peak in CMS decreased significantly due to the modification of AuNPs.

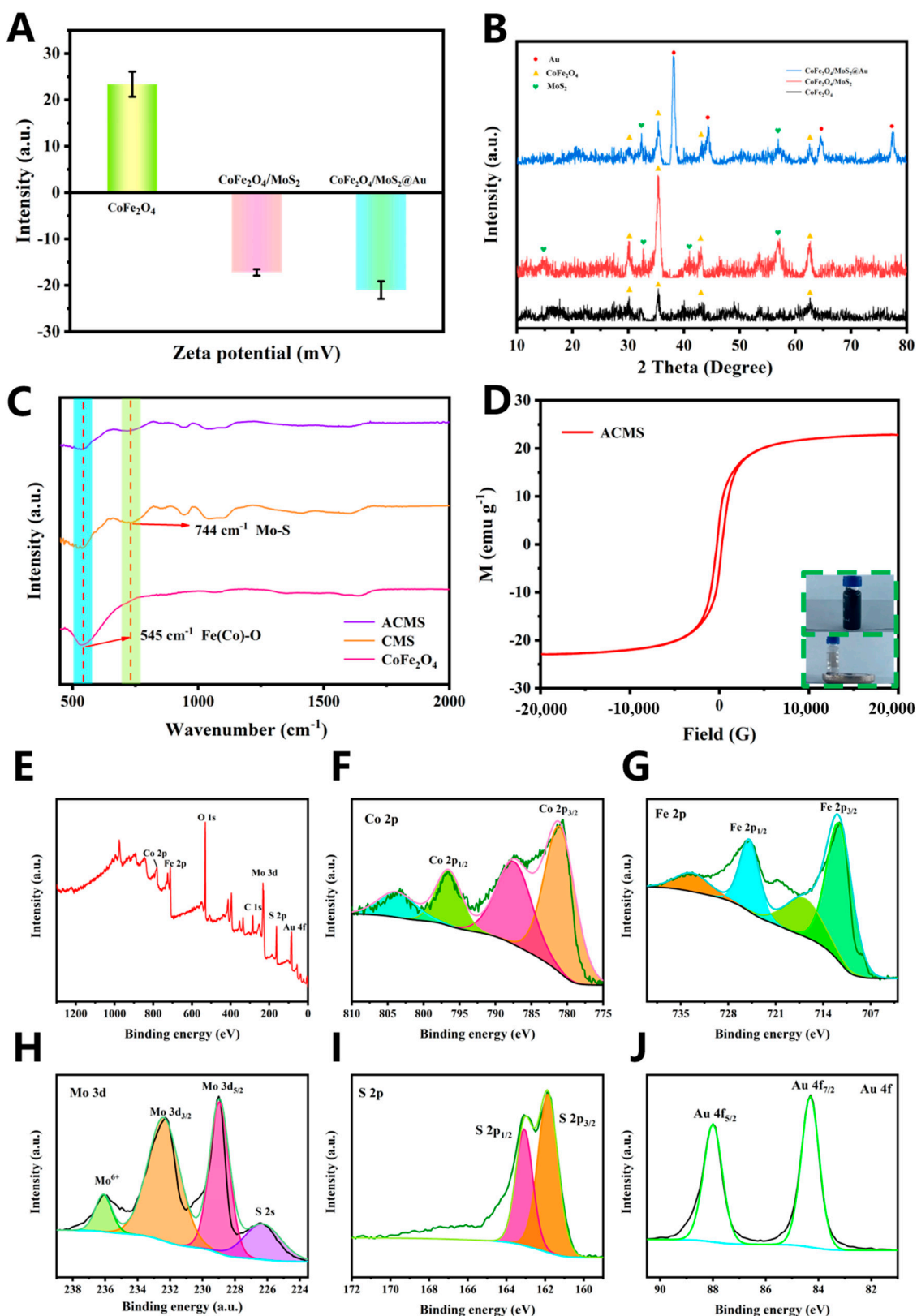


Figure 2. (A) Zeta potential of CoFe₂O₄, CMS and ACMS. (B) XRD patterns of CoFe₂O₄, CMS and ACMS. (C) The FT-IR spectra of CoFe₂O₄, CMS and ACMS. (D) The VSM of ACMS. XPS spectra of ACMS, (E) survey, (F) Co 2p, (G) Fe 2p, (H) Mo 3d, (I) S 2p, and (J) Au 4f.

The FT-IR spectra were utilized to record the surface functional groups of as-synthesized materials. As presented in Figure 2C, all spectra possessed the characteristic peaks of 565 cm^{-1} , attributing to the Fe(Co)-O bond of CoFe_2O_4 . For CMS and ACMS, the peaks at 744 cm^{-1} belonged to the Mo-S bond. FT-IR spectra demonstrated the successful preparation of CoFe_2O_4 and CMS. In addition, it could be found that the spectra of ACMS and CMS were similar, indicating that the modification of AuNPs could not damage the structure of CMS. Furthermore, the introduction of CoFe_2O_4 provided magnetic properties for the heterojunction, which could realize the solid-liquid separation conveniently. And the magnetization hysteresis loop was determined to evaluate the magnetic saturation (Ms) of the as-prepared material. As presented in Figure 2D, the Ms value of ACMS heterojunction was 22.83 emu g^{-1} , indicating that the materials proposed superior magnetism. Thus, the ACMS heterojunction could be separated conveniently in the presence of external magnetic fields (inset picture of Figure 2D).

The binding energy and elemental component of ACMS were examined by XPS. The survey spectra of ACMS (Figure 2E) illustrated the existence of Au, Mo, S, Fe, O, and Co elements in ACMS heterojunction. As for ACMS, the characteristic peaks at 796.6 eV and 781.3 eV corresponded to Co $2p_{1/2}$ and Co $2p_{3/2}$, respectively (Figure 2F). And two major peaks attributed to Fe $2p_{3/2}$ and Fe $2p_{1/2}$ could be observed at 711.9 and 724.9 eV, respectively (Figure 2G). In the high-resolution spectra of Mo 3d, the peaks centered at 232.4 and 229 eV (with spin-energy separation of 3.4 eV) could be ascribed to Mo $3d_{3/2}$ and Mo $3d_{5/2}$, which resulted from the spin-orbit characteristic of Mo^{4+} (Figure 2H). And the two peaks at 161.8 and 163.1 eV were distributed to the binding energies of S $3p_{3/2}$ and S $3d_{1/2}$, respectively (Figure 2I). Meanwhile, two definite peaks located at 87.9 and 84.3 eV were the satellite peaks of Au $4f_{5/2}$ and Au $4f_{7/2}$, respectively (Figure 2J).

3.2. Photocatalytic Activities

Firstly, crystal violet was chosen to appraise the photocatalytic capability of as-fabricated materials. As depicted in Figure 3A, CMS displayed a steady decrease tendency, and its photocatalytic degradation rate could reach 80.59% within 90 min. Compared to bare CoFe_2O_4 and MoS_2 , the CMS and ACMS composites exhibited a much higher degradation rate, ascribing to the construction of heterostructure and enhancement of light absorption [22]. In the presence of ACMS composites, it could be observed that the degradation rate of CV could reach 94.76% with the simulated solar light irradiation. Compared with previously reported Z-scheme heterojunctions as seen in Table 1, it was found that the degradation capability of ACMS composite is higher than other Z-scheme heterojunctions. And the kinetic behaviors of the materials for the photodegradation of CV were roughly conformed to the Langmuir-Hinshelwood kinetic model:

$$-\ln(C/C_0) = kt \quad (3)$$

where k refers to the rate constant. The k value for photodegradation CV with different photocatalysts was presented in Figure 3B. ACMS exhibited 1.714 times greater photodegradation rate constant (0.03061 min^{-1}) than that of CMS (0.01754 min^{-1}). In addition, the recirculation experiments were also carried out to estimate the reusability of ACMS heterojunction. As depicted in Figure 3C, the degradation efficiency of ACMS heterojunction still remained at 91.95% after 3 cycles under simulated solar light irradiation. To illustrate the possible influence on the crystal structure of ACMS heterojunction by the photodegradation tests, XRD characterization was performed after the recirculation. As seen in Figure 3D, the crystal phase of the materials maintained the same as ACMS before the reaction.

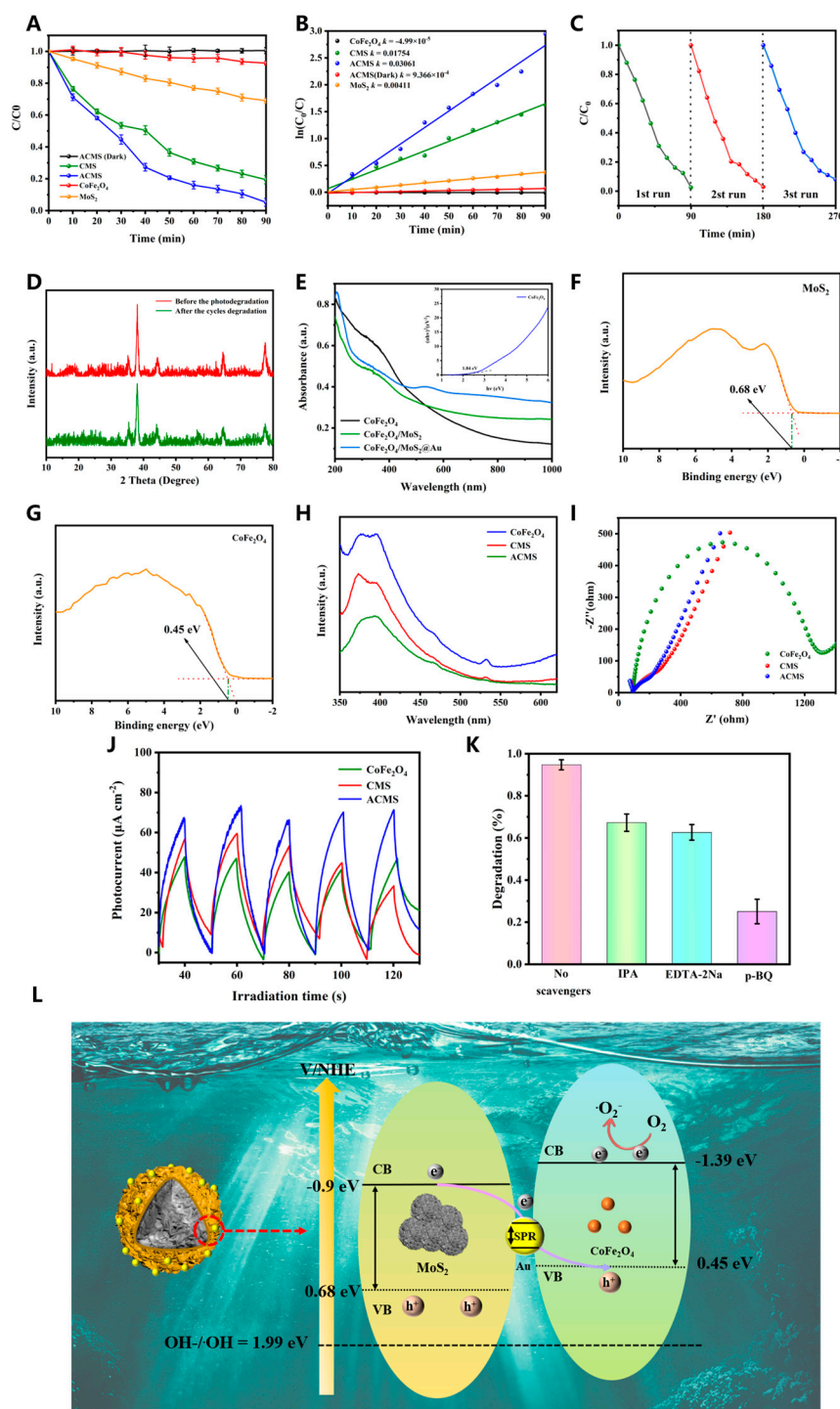


Figure 3. (A) The photocatalytic degradation of CV with as-prepared materials under simulated light irradiation. (B) The corresponding kinetic curves of photocatalytic degradation rate. (C) Recycling photocatalytic degradation of CV tests of ACMS. (D) The XRD patterns of ACMS before and after photodegradation. (E) UV-vis spectra as well as Tauc plots of the as-prepared samples. The XPS valence band spectra of (F) MoS₂ and (G) CoFe₂O₄, respectively. (H) PL spectra of as-synthesized samples. (I) Electrical impedance spectra of the samples of CoFe₂O₄, CMS and ACMS. (J) Transient photocurrent response of CoFe₂O₄, CMS and ACMS. (K) Photocatalytic activity of the ACMS heterojunction for the degradation of CV with different scavengers. (L) Schematic description of the photocatalytic mechanism of ACMS.

Table 1. Comparison of degradation of contaminants by Z-scheme heterojunction.

Substrate	Targets/Concentration	Catalytic Conditions	Recovery Time	Ref.
30% In ₂ S ₃ /Bi ₂ WO ₆	Tetracycline hydrochloride, 20 mg/L	Visible light	96.0%, 120 min	[23]
Bi ₃ O ₄ Cl/Bi ₂ MoO ₆	Norfloxacin, 10 mg/L	Visible light	87.34%, 150 min	[24]
Bi ₂ S ₃ /SnS ₂ /Bi ₂ O ₃	CV, 5 mg/L	Visible light	90 min, 99.6%	[25]
Fe ₂ O ₃ /GO/WO ₃	CV, 20 mg/L	Solar light	95.4%, 120 min	[26]
ACMS	CV, 37.5 mg/L	Solar light	94.76%, b90 min	This work

3.3. Photoelectric Properties of Samples

In order to further verify improved photocatalytic capability, a series of photoelectric properties of as-prepared materials were detected. As seen in Figure 3E, ACMS exhibited the best light absorption ability due to the SPR effect. And the bandgap of CoFe₂O₄ was determined utilizing the Kubelka–Munk equation [11]:

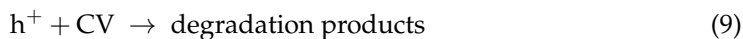
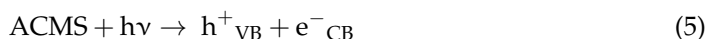
$$(\alpha h\nu)^2 = A(h\nu - E_g) \quad (4)$$

where α = absorption coefficient, h = Planck's constant, E_g is the allowed energy gap, A = absorption coefficient, ν = light frequency. As depicted in the inset picture of Figure 3E, the bandgap of CoFe₂O₄ was calculated as 1.84 eV, which agreed with the previous reports [27]. Meanwhile, the bandgap of MoS₂ was concluded as 1.58 eV as our previous research [18]. As seen in the XPS valence band (VB) spectra (Figure 3F,G), the VB was evaluated to be at 0.45 and 0.68 eV for CoFe₂O₄ and MoS₂, respectively. Thus, the conduction bands (CB) of CoFe₂O₄ and MoS₂ could be calculated as -1.39 eV and -0.9 eV, respectively.

The recombination of photogenerated carriers was related to the PL intensity. As reported previously, the PL intensities are proportional to the separation efficiency of photoexcited carriers [28]. Thus, the PL spectra were performed to estimate the photocatalytic activity of as-synthesized materials. As exhibited in Figure 3H, pure CoFe₂O₄ possessed the highest PL intensity due to the rapid recombination rate of photoexcited carriers. Furthermore, the PL intensities of CMS and ACMS heterojunction reduced significantly, implying that the photoexcited holes and electrons were separated because of the fabrication of heterostructure. In order to further investigate the migration efficiency of photoexcited carriers, the EIS spectrum was carried out to evaluate the charge transfer capability of as-synthesized materials. It is well known that the bigger arc radius reflected the lower charge transfer capacity [29]. The arc radius of the photocatalysts followed an order of CoFe₂O₄ > CMS > ACMS, indicating that the ACMS exhibited the best separation ability of photogenerated carriers. In addition, the photocurrent response depended on the excitation of the carriers (Figure 3I) [30]. From Figure 3J, all materials obtained a certain photocurrent response capability while the light was turned on, indicating that as-prepared photocatalysts obtained different photogenerated carriers' generation efficiency. Compared with the CoFe₂O₄ and CMS composites, the photocurrent density of the ACMS enhanced significantly, ascribing to the facilitation of absorption and the migration of photogenerated carries.

To detect the dominating free radicals in the photodegradation reaction, EDTA-2Na, p-BQ and IPA were selected as scavengers of the hole (h^+), superoxide radical ($\bullet O_2^-$) and hydroxyl radical ($\bullet OH$), respectively [31]. As depicted in Figure 3K, it can be found that the CV degradation was inhibited significantly with the existence of p-BQ, indicating that superoxide radicals are essential to photocatalytic degradation, while the photodegradation efficiency of CV decreased slightly in the presence of EDTA-2Na and IPA, indicating that hydroxyl radicals and photogenerated holes had a certain influence in the photocatalytic process. It was a remarkable fact that the photocatalytic degradation of CV relied on superoxide radicals primarily, followed by holes and hydroxyl radicals.

According to the aforementioned results, a possible photodegradation mechanism of CV by ACMS heterojunction was proposed. As presented in Figure 3L, photogenerated electrons were excited from the valence band (VB) of both $CoFe_2O_4$ and MoS_2 and transferred to the corresponding conduction band (CB) when the materials accepted the photons. Because the MoS_2 nanoflower was covered with $CoFe_2O_4$ and AuNPs tightly, the photoexcited electrons on the CB of MoS_2 could migrate to the VB of $CoFe_2O_4$ and recombine with the holes. Therefore, the recombination of photoexcited carriers was inhibited significantly. The electrons on CB of $CoFe_2O_4$ could fabricate superoxide radicals via the reduction of O_2 , and the holes on VB of MoS_2 could participate in the degradation of CV directly. The photodegradation pathway was presented in the following formulas:



3.4. Water Remediation and Phytotoxicity Tests of ACMS in Water

According to the above tests, ACMS can photodegrade CV in water effectively, and the safety of ACMS-treated water was evaluated by the seed germination experiment. As seen in Figure 4A and Table 2, the growth of the vigna radiata seeds was significantly inhibited in the CV-contaminated water due to the toxicity of CV. Specifically, the seed germination rate (SGR) of vigna radiata seeds exposed to the CV-contaminated water (93.75%) was lower than that of uncontaminated water (100%) and ACMS-treated water (100%). And the seed germination index (SGI) of seeds was calculated as 1, 0.2819, and 0.9641 in the uncontaminated water, CV-contaminated water, and ACMS-treated water, respectively. As a result, the CV in the water was toxic to the germination of vigna radiata seeds. As seen in v and vi of Figure 4B, CV molecules could be translated from roots to stems and further inhibited the germination or growth of vigna radiata seeds. While the phytotoxicity of CV-contaminated water could be decreased significantly by ACMS treatment (iii and iv of Figure 4B). Thus, the ACMS could be applied to remediate the fungicide-polluted water [32].

Table 2. The ARL, SGR and SGI with different infusion solutions.

Samples	Average Root Length (cm)	Germination Rate	Germination Index
Water	8.7125	100	1
Treated wastewater	8.4	100	0.9641
CV solution	2.456	93.75	0.2819

ARL = average root lengths, SGR = seed germination rate, and SGI = seed germination index.

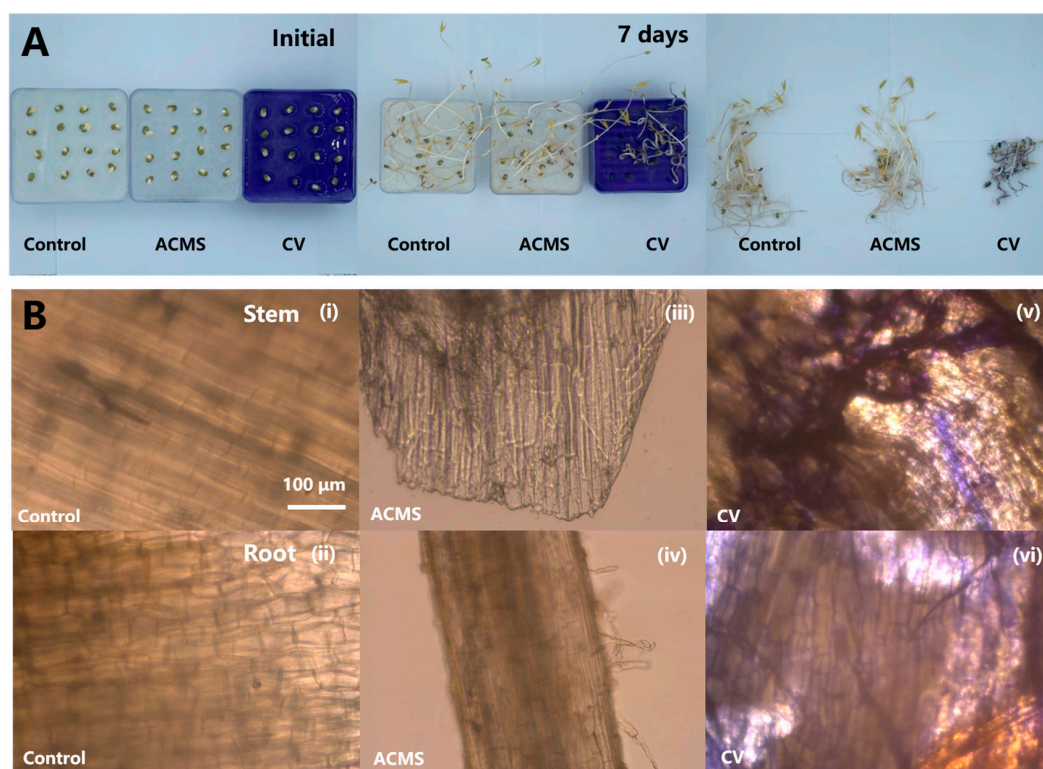


Figure 4. (A) *Vigna radiata* seeds showing the comparison of growth in different water, involving non-contaminated water (control), CV-contaminated water treated by ACMS (treatment), and CV-contaminated water. (B) Tissue slice graphs of different parts of *Vigna radiata*.

3.5. SERS Performance of ACMS

The SERS activity of the ACMS heterojunction was examined as a function of the amount of CMS and the time of ultrasonic deposition. The SERS intensity of CV (0.1 mg L^{-1}) at 1615 cm^{-1} shown in Figure 5A clearly demonstrated that the most appropriate ultrasonic deposition time was 30 min. The intensity of peaks was decreased significantly while the ultrasonic deposition time exceeded 30 min, which might be ascribed to AuNPs aggregation. Meanwhile, the optimal amount of CMS was selected as 5 mg (Figure 5B).

Meanwhile, CV was chosen as the SERS label to investigate the reproducibility of ACMS heterojunction. Figure 5C indicated that SERS spectra exhibited characteristic peaks at 1172 cm^{-1} (in-plane ring C–H bending) and 1615 cm^{-1} (C–C aromatic rings stretching) [33]. The SERS intensity decreased with the decrement of the concentration gradient, and the signal could be distinguished even at a concentration of as low as 0.001 mg L^{-1} . In addition, the SERS intensity at 1615 cm^{-1} , together with the CV concentration, was utilized to plot the linear curve and conclude with satisfied coefficients of determination (R^2) of 0.972 (Figure 5D). The enhancement factor of ACMS heterojunction was concluded to be 1.46×10^5 as the following equation (Figure 5E).

$$EF = \frac{I_{SERS}/N_{SERS}}{I_{Raman}/N_{Raman}} \quad (10)$$

Here, I_{SERS} and I_{Raman} are the SERS intensities of CV absorbed on the ACMS heterojunction and normal Raman of CV without any substrate, respectively. And N_{SERS} and N_{Raman} present CV molecule numbers for SERS and normal Raman detection, respectively. Furthermore, the uniformity test was carried out by measuring the SERS spectra of CV on 45 randomly selected spots in five groups of ACMS heterojunctions. The related SERS spectra are depicted in Figure 5F. The relative standard deviation (RSD) of ACMS was concluded to be 7.305% (Figure 5G). Thus, the value of RSD was less than 20%, illustrating that the ACMS heterojunction was applicable to determine fungicides in water [34].

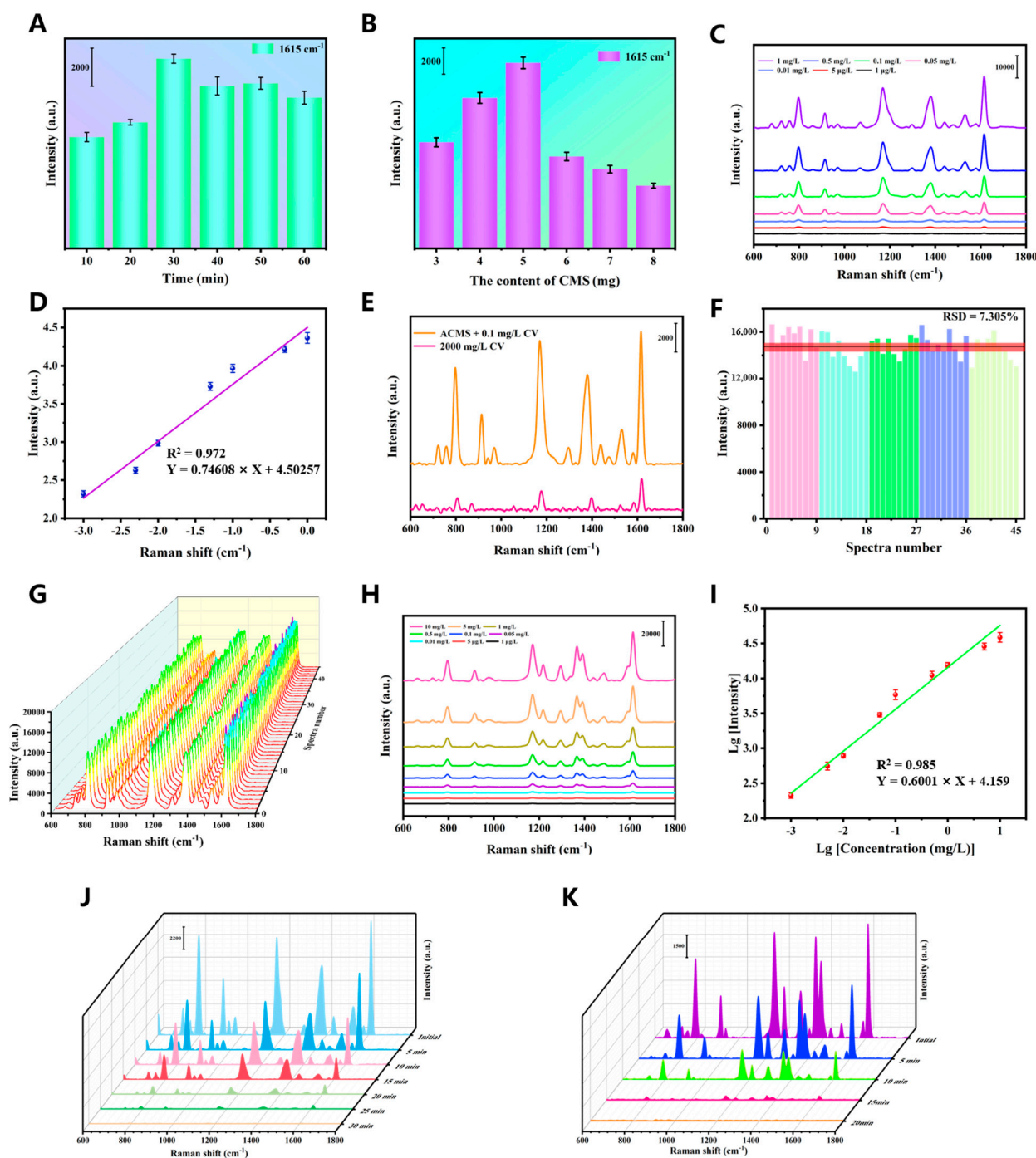


Figure 5. (A) Histogram of the peak intensities at 1615 cm^{-1} for CV by ACMS prepared with different ultrasonic times. (B) Histogram of the SERS intensities at 1615 cm^{-1} for CV by ACMS prepared with different amounts of CMS. (C) SERS determination of CV with different concentrations based on ACMS heterojunction. (D) Corresponding dose-response curves of the peak intensities at 1615 cm^{-1} for CV. (E) Raman spectra of CV (2 g/L) without substrate and the SERS spectra of CV solution (0.1 mg/L) based on ACMS heterojunction. (F) SERS spectra of CV and (G) SERS intensity at 1615 cm^{-1} collected from 45 random points in five batches of ACMS heterojunction. (H) SERS spectra of MG residues with different concentrations. (I) Corresponding dose-response curves of the peak intensities at 1618 cm^{-1} for MG. SERS spectra in situ recorded during the photodegradation process of (J) CV and (K) MG.

Figure 5H exhibited that the ACMS heterojunction responded well to the MG molecule, and the SERS peak intensities of MG increased with the MG concentration rising from 0.0001 to 10 mg L⁻¹. The observation of Figure 5I indicated that the logarithmic SERS intensities at 1618 cm⁻¹ (ring C–C stretching) obtained a good linear relation with the logarithmic concentration of MG, with an R² of 0.985. The LOD value was calculated as the following equation:

$$\text{LOD} = 3S_b + Y_b \quad (11)$$

Here, S_b refers to the standard deviation of Raman intensities, while Y_b denotes the average intensity of the corresponding wavenumber in the blank samples. And the LOD of ACMS for the determination of MG in water was concluded to be $4.309 \times 10^{-2} \mu\text{g L}^{-1}$. These results illustrated the excellent detection sensitivity of ACMS heterojunction to fungicides in water.

3.6. In Situ Photodegradation Monitoring

The photocatalytic process monitoring is essential to the piratical utilization of heterojunction for food safety control [10]. And the aforementioned tests testified that the ACMS exhibited good SERS capability and photocatalytic performance. Therefore, the ACMS heterojunction was utilized for in situ monitoring of the photodegradation process. As seen in Figure 5J, strong SERS signals of CV could be observed initially while no noticeable Raman peaks were detected after 30 min of simulated light irradiation, indicating that the CV molecules were photodegraded completely. In addition, Figure 5K showed that the photocatalytic rate of MG adsorbed on ACMS could reach approximately 100% within 20 min.

3.7. Detection of MG in Crucian Carp Samples

To estimate the practical application capability of the ACMS heterojunction, the fungicides determination in crucian carp extract based on as-prepared material was carried out. As seen in Table 3, crucian carp extract with different concentrations of MG were utilized as practical samples for SERS analysis, resulting in a recovery rate of 96.00~116.40%. Therefore, the aforementioned results indicated that the ACMS heterojunction exhibited broad prospects in determining food contaminants.

Table 3. Detection of fungicides in the extract of crucian carp extract.

Sample	Added Mount (mg/kg)	Detected ^a ± SD ^b (mg/kg)	Recovery (%)
1	0.5	0.528 ± 0.039	105.60
2	0.1	0.116 ± 0.051	116.00
3	0.05	0.048 ± 0.009	96.00

^a Mean of three determinations. ^b SD: standard deviation.

4. Conclusions

In summary, ACMS multifunction composites were synthesized via hydrothermal and ultrasonic sedimentation strategies for aquatic food safety control. The results illustrated that the as-synthesized heterojunction exhibited excellent photocatalytic capability with a degradation rate of 94.76% for CV photocatalytic degradation under simulated solar light irradiation, which could be attributed to the construction of Z-scheme heterostructure. In addition, such multifunction material was utilized to detect the MG residues in water, resulting in an LOD of $4.309 \times 10^{-2} \mu\text{g L}^{-1}$. And the ACMS composites were also performed in the determination of MG in crucian carp extract, with a recovery rate of 96.00~116.00%. Moreover, the multifunction ACMS platform was carried out for in situ monitoring of the degradation process, which is promising to be widely applied in comprehensive aquatic food safety control.

Author Contributions: Q.D.: Writing—original draft, Formal analysis, Investigation. Q.W.: Supervision, Validation, Funding acquisition, Resources. H.P.: Validation, Funding acquisition, Resources Supervision, Funding acquisition, Resources—review & editing. All authors have read and agreed to the published version of the manuscript.

Funding: This research was funded by the Guangdong Basic and Applied Basic Research Foundation (2022A1515012489), the International S&T Cooperation Projects of Guangdong Province (2022A0505050003), the National Natural Science Foundation of China (3217161084) and the Common Technical Innovation Team of Guangdong Province on Preservation and Logistics of Agricultural Products (2023KJ145).

Data Availability Statement: Data are available within the article.

Acknowledgments: Thank you to Tang Zhenghua for your support in fabrication of nanoparticle materials.

Conflicts of Interest: The authors declare no conflict of interest.

References

1. Qiang, T.; Chen, L.; Xia, Y.; Qin, X. Dual modified MoS₂/SnS₂ photocatalyst with Z-scheme heterojunction and vacancies defects to achieve a superior performance in Cr (VI) reduction and dyes degradation. *J. Clean. Prod.* **2021**, *291*, 125213. [[CrossRef](#)]
2. Shen, K.; Cui, Y.; Zhang, D.; Liu, M.; Huang, H.; Sha, X.; Deng, F.; Zhou, N.; Zhang, X.; Wei, Y. Biomimetic preparation of MoS₂-Fe₃O₄ MNPs as heterogeneous catalysts for the degradation of methylene blue. *J. Environ. Chem. Eng.* **2020**, *8*, 104125. [[CrossRef](#)]
3. Lai, H.; Ma, G.; Shang, W.; Chen, D.; Yun, Y.; Peng, X.; Xu, F. Multifunctional magnetic sphere-MoS₂@Au hybrid for surface-enhanced Raman scattering detection and visible light photo-Fenton degradation of aromatic dyes. *Chemosphere* **2019**, *223*, 465–473. [[CrossRef](#)] [[PubMed](#)]
4. Chen, Y.; Liu, H.; Tian, Y.; Du, Y.; Ma, Y.; Zeng, S.; Gu, C.; Jiang, T.; Zhou, J. In Situ Recyclable Surface-Enhanced Raman Scattering-Based Detection of Multicomponent Pesticide Residues on Fruits and Vegetables by the Flower-like MoS₂@Ag Hybrid Substrate. *ACS Appl. Mater. Interfaces* **2020**, *12*, 14386–14399. [[CrossRef](#)] [[PubMed](#)]
5. Mai, H.; Chen, D.; Tachibana, Y.; Suzuki, H.; Abe, R.; Caruso, R.A. Developing sustainable, high-performance perovskites in photocatalysis: Design strategies and applications. *Chem. Soc. Rev.* **2021**, *50*, 13692–13729. [[CrossRef](#)]
6. Jo, W.-K.; Lee, J.Y.; Selvam, N.C.S. Synthesis of MoS₂ nanosheets loaded ZnO–g-C₃N₄ nanocomposites for enhanced photocatalytic applications. *Chem. Eng. J.* **2016**, *289*, 306–318. [[CrossRef](#)]
7. Jiang, Q.-Y.; Li, D.; Liu, Y.; Mao, Z.-S.; Yu, Y.; Zhu, P.; Xu, Q.; Sun, Y.; Hu, L.; Wang, J.; et al. Recyclable and green AuBPs@MoS₂@tin foil box for high throughput SERS tracking of diquat in complex compounds. *Sens. Actuators B Chem.* **2021**, *344*, 130290. [[CrossRef](#)]
8. Zhou, H.; Lai, L.; Wan, Y.; He, Y.; Yao, G.; Lai, B. Molybdenum disulfide (MoS₂): A versatile activator of both peroxymonosulfate and persulfate for the degradation of carbamazepine. *Chem. Eng. J.* **2020**, *384*, 123264. [[CrossRef](#)]
9. Govarthan, M.; Mythili, R.; Kim, W.; Alfarraj, S.; Alharbi, S.A. Facile fabrication of (2D/2D) MoS₂@MIL-88(Fe) interface-driven catalyst for efficient degradation of organic pollutants under visible light irradiation. *J. Hazard. Mater.* **2021**, *414*, 125522. [[CrossRef](#)]
10. Quan, Y.; Su, R.; Yang, S.; Chen, L.; Wei, M.; Liu, H.; Yang, J.; Gao, M.; Li, B. In-situ surface-enhanced Raman scattering based on MTi₂₀ nanoflowers: Monitoring and degradation of contaminants. *J. Hazard. Mater.* **2021**, *412*, 125209. [[CrossRef](#)]
11. Yang, Y.; Gong, W.; Li, X.; Liu, Y.; Liang, Y.; Chen, B.; Yang, Y.; Luo, X.; Xu, K.; Yuan, C. Light-assisted room temperature gas sensing performance and mechanism of direct Z-scheme MoS₂/SnO₂ crystal faceted heterojunctions. *J. Hazard. Mater.* **2022**, *436*, 129246. [[CrossRef](#)] [[PubMed](#)]
12. Liu, Z.; Liu, Y.; Sun, X.; Ji, H.; Liu, W.; Cai, Z. Construction of Z-scheme Ag/AgVO₃/carbon-rich g-C₃N₄ heterojunction for enhanced photocatalytic degradation of sulfamethiazole: DFT calculation and mechanism study. *Chem. Eng. J.* **2022**, *433*, 133604. [[CrossRef](#)]
13. Hassani, A.; Eghbali, P.; Mahdipour, F.; Waclawek, S.; Lin, K.-Y.A.; Ghanbari, F. Insights into the synergistic role of photocatalytic activation of peroxymonosulfate by UVA-LED irradiation over CoFe₂O₄-rGO nanocomposite towards effective Bisphenol A degradation: Performance, mineralization, and activation mechanism. *Chem. Eng. J.* **2023**, *453*, 139556. [[CrossRef](#)]
14. Feng, S.; Yu, M.; Xie, T.; Li, T.; Kong, D.; Yang, J.; Cheng, C.; Chen, H.; Wang, J. MoS₂/CoFe₂O₄ heterojunction for boosting photogenerated carrier separation and the dominant role in enhancing peroxymonosulfate activation. *Chem. Eng. J.* **2022**, *433*, 134467. [[CrossRef](#)]
15. Liu, Z.; Xu, K.; Yu, H.; Sun, Z. Synergistic effect of Ag/MoS₂/TiO₂ heterostructure arrays on enhancement of photoelectrochemical and photocatalytic performance. *Int. J. Energy Res.* **2020**, *45*, 6850–6862. [[CrossRef](#)]
16. Zeng, Y.; Guo, N.; Song, Y.; Zhao, Y.; Li, H.; Xu, X.; Qiu, J.; Yu, H. Fabrication of Z-scheme magnetic MoS₂/CoFe₂O₄ nanocomposites with highly efficient photocatalytic activity. *J. Colloid Interface Sci.* **2018**, *514*, 664–674. [[CrossRef](#)]

17. Ren, B.; Shen, W.; Li, L.; Wu, S.; Wang, W. 3D CoFe₂O₄ nanorod/flower-like MoS₂ nanosheet heterojunctions as recyclable visible light-driven photocatalysts for the degradation of organic dyes. *Appl. Surf. Sci.* **2018**, *447*, 711–723. [[CrossRef](#)]
18. Wei, Q.; Dong, Q.; Sun, D.-W.; Pu, H. Synthesis of recyclable SERS platform based on MoS₂@TiO₂@Au heterojunction for photodegradation and identification of fungicides. *Spectrochim. Acta A Mol. Biomol. Spectrosc.* **2022**, *285*, 121895. [[CrossRef](#)]
19. Ahamad, T.; Naushad, M.; Al-Saeedi, S.I.; Almotairi, S.; Alshehri, S.M. Fabrication of MoS₂/ZnS embedded in N/S doped carbon for the photocatalytic degradation of pesticide. *Mater. Lett.* **2020**, *263*, 127271. [[CrossRef](#)]
20. Li, G.; Wang, R.; Wang, B.; Zhang, J. Sm-doped mesoporous g-C₃N₄ as efficient catalyst for degradation of tylosin: Influencing factors and toxicity assessment. *Appl. Surf. Sci.* **2020**, *517*, 146212. [[CrossRef](#)]
21. Hu, B.; Sun, D.-W.; Pu, H.; Wei, Q. A dynamically optical and highly stable pNIPAM@Au NRs nanohybrid substrate for sensitive SERS detection of malachite green in fish fillet. *Talanta* **2020**, *218*, 121188. [[CrossRef](#)]
22. Ibrahim, I.; Kaltzoglou, A.; Athanasekou, C.; Katsaros, F.; Devlin, E.; Kontos, A.G.; Ioannidis, N.; Perraki, M.; Tsakiridis, P.; Sygellou, L.; et al. Magnetically separable TiO₂/CoFe₂O₄/Ag nanocomposites for the photocatalytic reduction of hexavalent chromium pollutant under UV and artificial solar light. *Chem. Eng. J.* **2020**, *381*, 122730. [[CrossRef](#)]
23. He, Z.; Siddique, M.S.; Yang, H.; Xia, Y.; Su, J.; Tang, B.; Wang, L.; Kang, L.; Huang, Z. Novel Z-scheme In₂S₃/Bi₂WO₆ core-shell heterojunctions with synergistic enhanced photocatalytic degradation of tetracycline hydrochloride. *J. Clean. Prod.* **2022**, *339*, 130634. [[CrossRef](#)]
24. Liu, J.; Jiang, L.; Zhang, H.; Yao, H.; Chai, J.; Wang, J.; Fang, D.; Zhang, Z.; Tie, M. Construction of high-proportion dual bismuth-based Z-scheme Bi₃O₄Cl/Bi₂MoO₆ photocatalytic system via in-situ growth of Bi₂MoO₆ on Bi₃O₄Cl for enhanced photocatalytic degradation of organic pollutants. *J. Alloys Compd.* **2023**, *956*, 170375. [[CrossRef](#)]
25. Yu, C.; Wang, K.; Yang, P.; Yang, S.; Lu, C.; Song, Y.; Dong, S.; Sun, J.; Sun, J. One-pot facile synthesis of Bi₂S₃/SnS₂/Bi₂O₃ ternary heterojunction as advanced double Z-scheme photocatalytic system for efficient dye removal under sunlight irradiation. *Appl. Surf. Sci.* **2017**, *420*, 233–242. [[CrossRef](#)]
26. Mohamed, H.H. Rationally designed Fe₂O₃/GO/WO₃ Z-Scheme photocatalyst for enhanced solar light photocatalytic water remediation. *J. Photochem. Photobiol. A Chem.* **2019**, *378*, 74–84. [[CrossRef](#)]
27. Ferdosi, E.; Bahiraei, H.; Ghanbari, D. Investigation the photocatalytic activity of CoFe₂O₄/ZnO and CoFe₂O₄/ZnO/Ag nanocomposites for purification of dye pollutants. *Sep. Purif. Technol.* **2019**, *211*, 35–39. [[CrossRef](#)]
28. Chen, L.; Tsai, M.-L.; Chuang, Y.; Chen, C.-W.; Dong, C.-D. Construction of carbon nanotubes bridged MoS₂/ZnO Z-scheme nanohybrid towards enhanced visible light driven photocatalytic water disinfection and antibacterial activity. *Carbon* **2022**, *196*, 877–889. [[CrossRef](#)]
29. Wang, Y.; Xing, Z.; Zhao, H.; Song, S.; Liu, M.; Li, Z.; Zhou, W. MoS₂@In₂S₃/Bi₂S₃ Core-shell dual Z-scheme tandem heterojunctions with Broad-spectrum response and enhanced Photothermal-photocatalytic performance. *Chem. Eng. J.* **2022**, *431*, 133355. [[CrossRef](#)]
30. Mandal, S.; Adhikari, S.; Choi, S.; Lee, Y.; Kim, D.-H. Fabrication of a novel Z-scheme Bi₂MoO₆/GQDs/MoS₂ hierarchical nanocomposite for the photo-oxidation of ofloxacin and photoreduction of Cr(VI) as aqueous pollutants. *Chem. Eng. J.* **2022**, *444*, 136609. [[CrossRef](#)]
31. Ma, E.; Sun, G.; Duan, F.; Wang, H.; Wang, H. Visible-light-responsive Z-scheme heterojunction MoS₂ NTs/CuInS₂ QDs photoanode for enhanced photoelectrocatalytic degradation of tetracycline. *Appl. Mater. Today* **2022**, *28*, 101504. [[CrossRef](#)]
32. Zhang, Y.; Nie, S.; Nie, M.; Yan, C.; Qiu, L.; Wu, L.; Ding, M. Remediation of sulfathiazole contaminated soil by peroxymonosulfate: Performance, mechanism and phytotoxicity. *Sci. Total Environ.* **2022**, *830*, 154839. [[CrossRef](#)] [[PubMed](#)]
33. Zhai, Y.; Yang, H.; Zhang, S.; Li, J.; Shi, K.; Jin, F. Controllable preparation of the Au–MoS₂ nano-array composite: Optical properties study and SERS application. *J. Mater. Chem. C* **2021**, *9*, 6823–6833. [[CrossRef](#)]
34. Wang, K.; Sun, D.W.; Pu, H.; Wei, Q. Polymer multilayers enabled stable and flexible Au@Ag nanoparticle array for nondestructive SERS detection of pesticide residues. *Talanta* **2021**, *223*, 121782. [[CrossRef](#)] [[PubMed](#)]

Disclaimer/Publisher’s Note: The statements, opinions and data contained in all publications are solely those of the individual author(s) and contributor(s) and not of MDPI and/or the editor(s). MDPI and/or the editor(s) disclaim responsibility for any injury to people or property resulting from any ideas, methods, instructions or products referred to in the content.